Sonochemical synthesis of dual phase $Y_2SiO_5:Eu^{3+}$ nanopowder: luminescence and Judd-Ofelt analysis

M. Mangala Gowri, R.B. Basavaraj, H. Nagabhushana*

Prof. C.N.R. Rao Centre for Advanced Materials Research, Tumkur University, Tumkur, 572 103, India

Abstract

$Y_2SiO_5:Eu^{3+}$ (1-9 mol %) nanopowders were prepared by sonochemical method and the obtained sample was calcined at 1100 ^{0}C and 1300 ^{o}C respectively. The product was well-characterized by Powder X-ray diffraction (PXRD), Photoluminescence (PL), diffuse reflectance spectral (DRS) studies etc. When the samples were calcined at 1100 ^{o}C, pure monoclinic X_1 phase was obtained, whereas, samples calcined at 1300 ^{o}C showed pure X_2 phase of Y_2SiO_5. The average crystallite size estimated by Debye–Scherrer's and Williamson–Hall plots were found to be in the range of 41-46 nm in X_1 phase, and 50-55 nm in X_2 phase. The effect of dopant concentration and calcination temperature on luminescence property was thoroughly investigated. CIE chromaticity coordinates were well located in red region. The average CCT values were estimated to ~ 1806 K and ~ 1776 K in X_1 and X_2 phases respectively. Colour purity, quantum efficiency were estimated for both the phases. The Judd-Ofelt intensity parameters were estimated and values of Ω_2, Ω_4 and Ω_6 were found to be 2.86, 4.20 and 0.13 in X_1 phase and 5.43, 2.29 and 0.07 in X_2 phase respectively in $10^{-20} cm^2$ units. The above results clearly exhibit that the nanophosphor prepared via sonochemical method were considered as potential candidates for applications in display devices.

Keywords: Photoluminescence; concentration quenching; Judd-Ofelt analysis, optical gain.

*Corresponding Author: E-mail address: bhushanvlc@gmail.com (Dr. H. Nagabhushana).

1. Introduction

Yttrium orthosilicate (YSO) has been proved to be an excellent host material for rare-earth elements due to its special properties such as water and chemical resistance, and visible light transparency [1]. Moreover, some of its properties with regard to its thermal stability; wide energy band gap; cost effectiveness; non-toxicity; chemical resistance; high temperature strength; low thermal expansion and high conductivity; multi-colour phosphorescence; and high resistance to acid, alkali and oxygen are noteworthy. Among silicate phosphors, YSO doped with rare-earth ions are studied extensively in display applications [2]. YSO has been proved to be an excellent cathodoluminescent material and when doped with Eu^{3+}, turns out to be a promising candidate for coherent time-domain optical memory and red phosphor for lamps and display applications [3-4].

Luminescence properties of Eu^{3+} doped compounds have been studied extensively in various forms of compounds such as solutions, polymer compounds, liquid crystals, glasses, etc. These compounds have been prepared via various conventional methods [5-8]. Silicate nanophosphors are synthesized by a variety of routes such as solid-state reactions [9], sol–gel [10], hydrothermal [11], co-precipitation [12] and spray pyrolysis [13]. It has also been established that the synthesis method and conditions influence the luminescence properties. In the present study, the Eu^{3+} doped (1-9 mol %) YSO nanophosphor was synthesized sonochemically. The prepared sample was calcined at 1100^{0}C and at 1300^{0}C. Due to quantum confinement effects incorporation of rare-earth trivalent cations to a host lattice, the properties of the nanophosphor is enhanced substantially. Eu^{3+} doped YSO phosphor emits in red region with appreciable colour purity. The nanophosphor is excited by near ultraviolet light. Extensive study of YSO:Eu^{3+} synthesized via sonochemical method has not been reported so far. This study is an effort to probe into the crystal structure of prepared nanophosphor by studying its photoluminescence.

2. Experimental

We used a typical laboratory-scale bath sonicator for the synthesis. Stoichiometric quantities

of yttrium nitrate (Sigma aldrich) and tetraethyl orthosilicate (Sigma aldrich) were dissolved in the distilled water and thoroughly mixed in a magnetic stirrer to get a uniform solution. Then the mixture was stirred ultrasonically (frequency ~ 20 kHz) at a fixed temperature of 75 ^{0}C. The solution was kept undisturbed until a white precipitate was formed. The precipitate was filtered. The obtained product was dried overnight in an oven at 100 ^{0}C. Further, the product was calcined at 1100 ^{0}C for 3 h in air atmosphere. As another attempt for the mixture of yttrium nitrate and tetraethyl orthosilicate, stoichiometric amount of europium nitrate (1-9 mol %) was added and stirred in a magnetic stirrer. Ultrasonification of the mixture was carried out for 90 minutes as it was done without doping. The solution was kept undisturbed until a white precipitate was formed. The precipitate was filtered. The obtained product was dried overnight in an oven at 100 ^{0}C. A part of the product was calcined at 1100 ^{0}C for 3 h in air atmosphere and another part was calcined at 1300 ^{0}C.

It is known that ultrasonic irradiation of aqueous liquids generates free radicals [14]. These radicals either recombine to form their original form or combine to produce H_2 and H_2O_2. They can also produce HO_2 by combining with O_2. These strong oxidants and reductants are utilized for various sonochemical reactions in aqueous solutions.

3. Results and discussion

3.1 Powder X Ray Diffraction (PXRD)

Fig. 1(a) and 1(b) show the PXRD patterns of Y_2SiO_5:Eu^{3+} (1-9 mol %) NPs synthesized by sonochemical method calcined at 1100 ^{0}C and 1300 ^{0}C respectively. The PXRD patterns of all the samples calcined at 1100 ^{0}C match with the monoclinic phase of Y_2SiO_5 of type X1, and those calcined at 1300 ^{0}C match with that of phase X2. These two phases are well matched with JCPDS card number 74-2011 and 52-1810 respectively. A slight shift of peaks towards higher θ value is observed. This may be attributed to the difference in ionic radii of host element and the dopant ion and hence a change in the lattice parameters. However, diffraction peaks do not shift with the concentration of Eu^{3+} ions in Y_2SiO_5. Doping of Eu^{3+} does not introduce secondary phases. It is evident that Eu^{3+} ions are homogeneously mixed and effectively doped in the host lattice in Y^{3+} sites. The lattice parameter calculated using the equation

$$d_{hkl} = \frac{1}{\sqrt{\frac{h^2}{a^2} + \frac{k^2}{b^2} + \frac{l^2}{c^2}}} \quad (1)$$

was found to be around 3 Å. The X-ray diffraction pattern exhibits peak broadening for the particle size less than about 100 nm. The observed line broadening can be used to calculate the average crystallite size of the phosphor [15]. The average crystallite size was estimated using Scherrer's relation

$$D = \frac{k\lambda}{\beta \cos\theta} \quad (2)$$

where k is constant (shape factor (k = 0.9); λ is the X- ray wavelength (0.15418 nm), β the full width at half maximum (FWHM) of the diffraction line and diffraction angle. The average crystallite size was also estimated using W-H plots [16]. The FWHM can be expressed as a linear combination of microstrain and crystallite size. The effects of microstrain and crystallite size on the FWHM can be expressed by the equation

$$\beta \cos\theta = \frac{0.9\lambda}{D} + 4\varepsilon \sin\theta \quad (3)$$

where β is the measured FWHM (in radians), θ is the Bragg angle of the peak, λ is the X-ray diffraction wavelength, ε is the strain associated with the

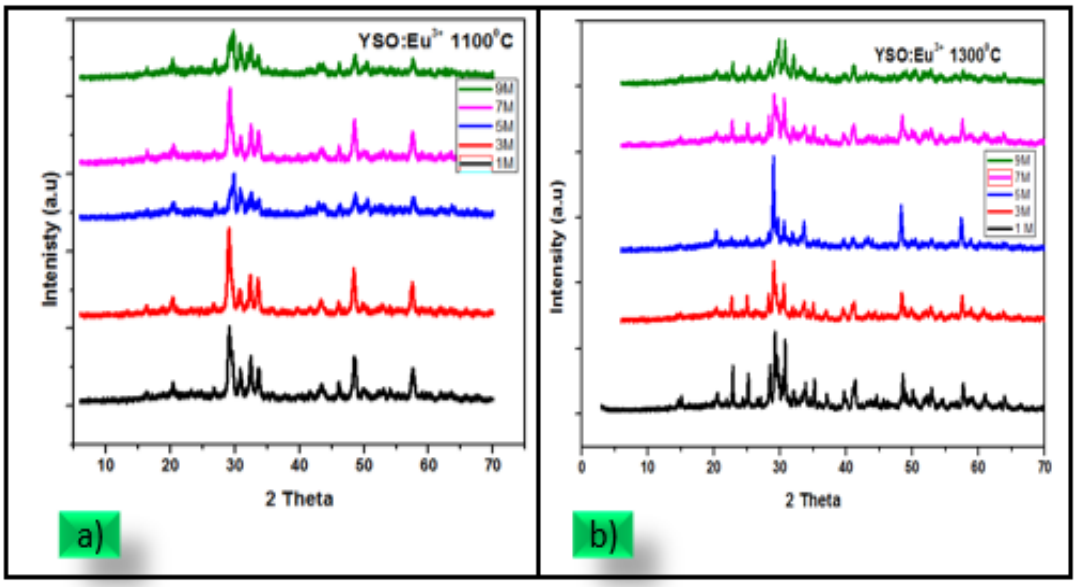

Fig. 1a) PXRD patterns of Y_2SiO_5:Eu^{3+} nanoparticles (1-9 mol %) a) calcined at 1100 ^{0}C b) calcined at 1300 ^{0}C

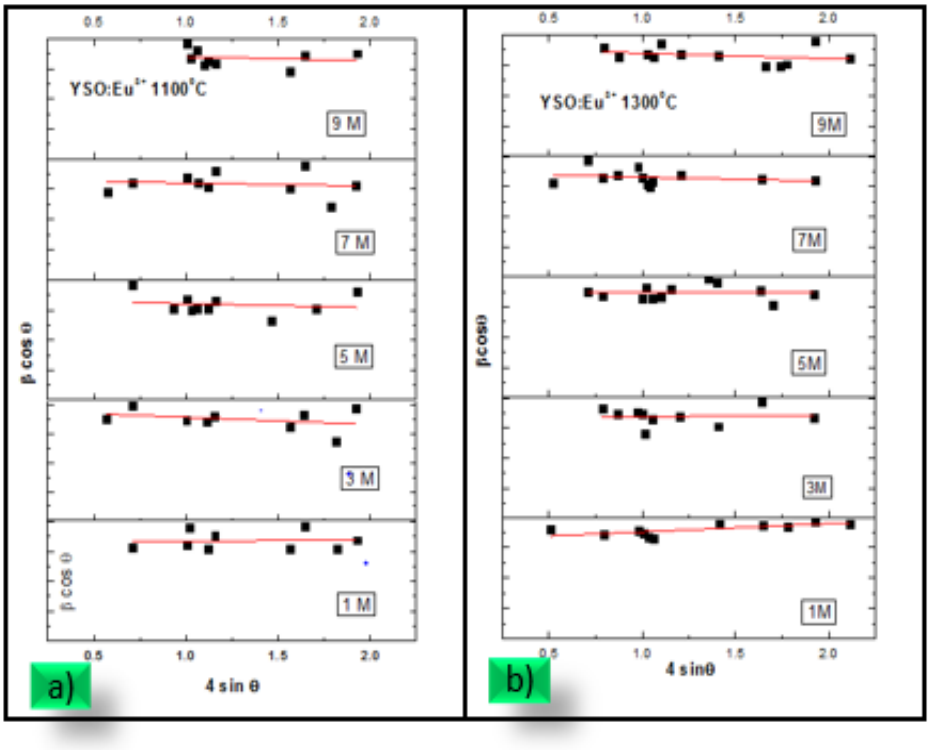

Fig. 2 W-H plots for $Y_2SiO_5:Eu^{3+}$ (1-9 mol %) NPs a) calcined at 1100 ^{0}C b) calcined at 1300 ^{0}C

nanoparticles. The above equation is a straight line if 4 sinθ is plotted along x-axis and βcosθ along the y-axis. Fig. 2(a) and 2(b) show the W-H plots of $Y_2SiO_5:Eu^{3+}$ (1-9 mol %) NPs calcined at 1100 ^{0}C and 1300 ^{0}C respectively. From the equation it is evident that the slope of line gives the strain (ε) and intercept (0.9λ/D) of this line on y-axis gives crystallite size (D).

The crystallite sizes of $Y_2SiO_5:Eu^{3+}$ (1-9 mol %) NPs calcined at 1100 ^{0}C were found to vary from 43-47 nm by Scherrer's and 40-42 nm by W-H plots method. Similarly, the crystallite sizes of $Y_2SiO_5:Eu^{3+}$ (1-9 mol %) NPs calcined at 1300 ^{0}C were found to vary from 50-60 nm by Scherrer's and 44-47 nm by W-H plot methods. An increase in strain is observed with the increase in Eu^{3+} concentration. The estimated crystallite size and strain values were tabulated in Table 1.

Table.1. Estimated crystallite size (Scherrer's formula and W - H method), strain of Y_2SiO_5: Eu^{3+} (1-9 mol %) NPs.

Eu^{3+} (mol%)	Calcination Temperature 1100 ^{0}C			Calcination Temperature 1300 ^{0}C		
	Crystallite size (nm)		Strain ($\times 10^{-4}$)	Crystallite size (nm)		Strain ($\times 10^{-4}$)
	Scherrer's	W-H		Scherrer's	W-H	
1	43.5	41.4	0.39	53.79	57.11	1.99
3	42.0	36.2	2.39	78.46	74.89	0.21
5	45.8	40.9	1.32	49.88	46.94	0.12
7	46.2	41.4	1.02	51.77	46.62	1.18
9	44.6	41.7	1.26	50.38	44.07	1.54

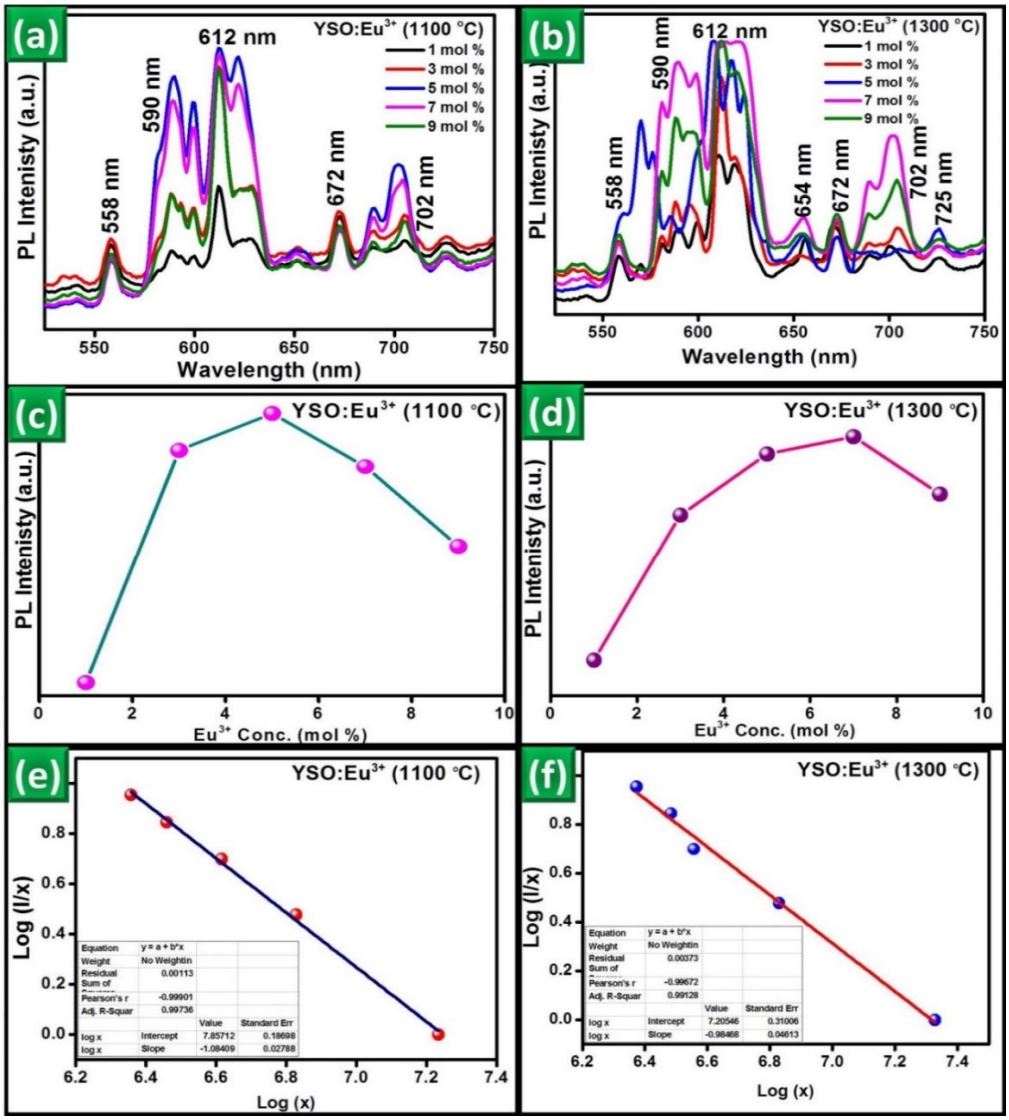

Fig. 3 PL Emission spectrum of $Y_2SiO_5:Eu^{3+}$ (1-9 mol %) NPs a) calcined at 1100 ^{0}C, b) calcined at 1300 ^{0}C, c) Variation of PL intensity with dopant concentration for $Y_2SiO_5:Eu^{3+}$ (1-9 mol %) NPs calcined at 1100 ^{0}C, d) calcined at 1300 ^{0}C, e) Plot of log(I/x) Vs log x for $Y_2SiO_5:Eu^{3+}$ (1-9 mol %) NPs calcined at 1100 ^{0}C, f) calcined at 1300 ^{0}C

3.2.Photoluminescence (PL)

The intensity of red emission corresponding to the transition $^5D_0 \rightarrow {}^7F_2$ is found to depend on the concentration of the dopant as illustrated in Fig. 3(c) and 3(d). It was found that the optimum concentration for bulk materials with large crystalline size is x=0.2 [17] .However, we have found that the maximum peak intensity for this transition was observed for 5 mol% of dopant concentration when calcined at 1100 ^{0}C and when calcined at 1300 ^{0}C the maximum peak intensity was observed for 7 mol% of Eu^{3+} concentration.

This effect may be due to concentration quenching phenomenon. The average distance between two neighboring dopant ions is influenced by concentration dopant. PL efficiency of a nanophospor depends on this critical distance between the activator ions [18]. High concentration may lead to non-radiative cross relaxation, and hence luminescence of the phosphor be quenched. The critical distance of energy transfer from one activator to the neighbouring ion is given by

$$R_C = 2\left[\frac{3V}{4\pi x_c N}\right]^{1/3} \quad (4)$$

Here V is the unit cell volume, N is the total Eu^{3+} sites per unit cell, and x_c is the critical concentration for energy transfer from one activator ion to the neighbouring ion. For the present nanophosphor calcined at 1100 ^{0}C, N=4, V=53.15Å^3, $x_c = 0.05$. The critical distance for energy transfer comes out to be $R_C = 7.98$ Å. And for the nanophosphor calcined at 1300 ^{0}C, the critical concentration was estimated to be, $x_c = 0.07$. And the critical distance of energy transfer comes out to be $R_C = 7.13$ Å. Since in both the cases R_C was not less than 5Å, exchange interaction was not responsible for non-radiative energy transfer process from one Eu^{3+} ion to another Eu^{3+} ion in this host .We did not observe broad overlapping peaks in the luminescence spectra. Thus, we conclude that radiative reabsorption is not the reason for the decrease in the intensity; rather a multipolar interaction (d-q) can be the cause of concentration quenching.

It was observed that the intensity (integrated intensity) of magnetic dipole transitions was more for lower dopant concentrations; however, it is less dominant than electric dipole transitions. This may be attributed to less polarizability of the compound with lower dopant concentration [19]. This can also be due to more emission from higher excited states when dopant concentration is low. Emission from higher excited states is suppressed as dopant concentration is increased.

Energy transfer due to electric multipolar interaction can be determined by the equation

$$\frac{I}{x} = k[1 + \beta(x)^{Q/3}]^{-1} \quad (5)$$

where I – the integral intensity of emission spectra, x –the activator concentration, I/x – the emission intensity per activator. Q, β and k – constants for a given host under same excitation condition. According to the above equation, $Q = 3$ for the energy transfer among the nearest neighbour ions, while $Q = 6, 8$ and 10 for d–d, d–q and q–q interactions respectively [20]. Q is determined by plotting logx vs. log (I/x) linear graph. For the compound calcined at 1100 ^{0}C the intercept was

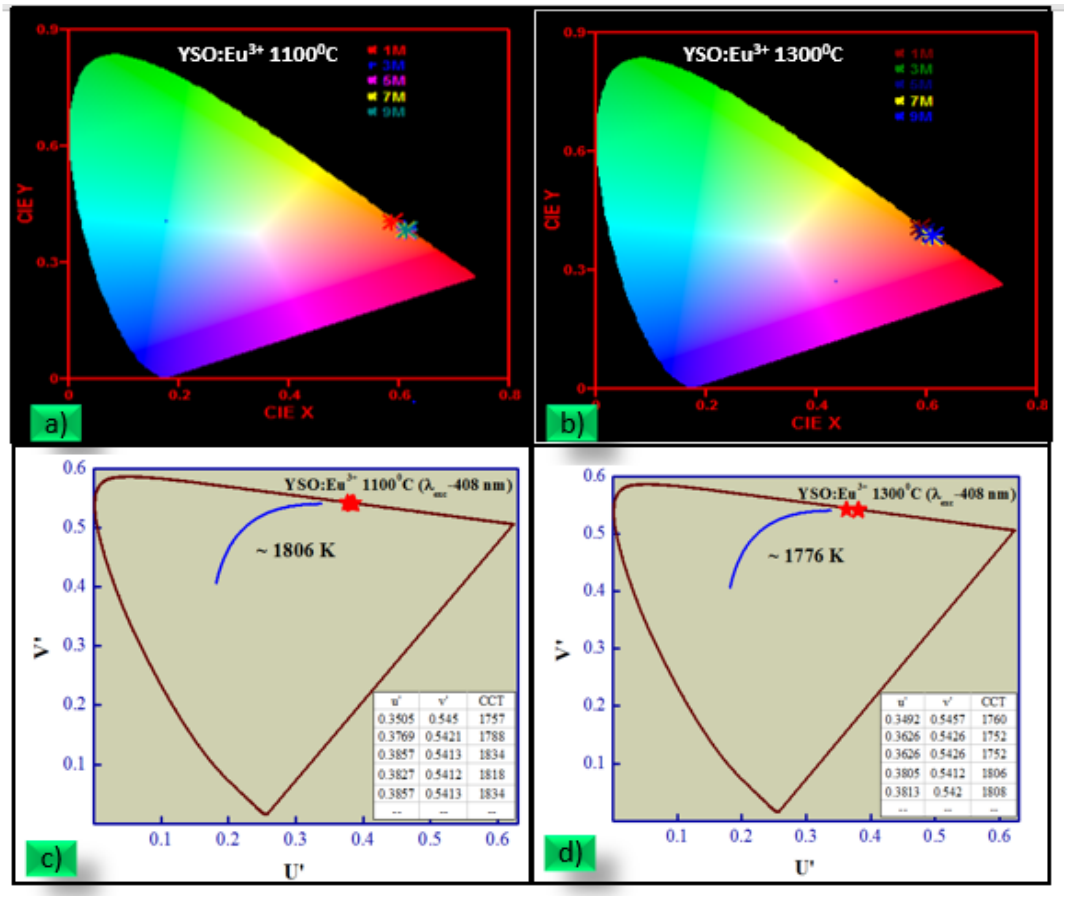

Fig. 4 CIE diagram of Y_2SiO_5:Eu $^{3+}$ (1-9 mol %) a) calcined at 1100 ^{0}C b) calcined at 1300 ^{0}C, CCT diagram of Y_2SiO_5:Eu $^{3+}$ (1-9 mol %) c) calcined at 1100 ^{0}C, d) calcined at 1300 ^{0}C

found as 7.85 and slope of -1.08 (Fig 3(e)). For the compound calcined at 1300 ^{0}C the intercept was found to be 7.205 and the slope is 0.985 (Fig. 3(f)). In both the cases the intercept can be approximated to $Q = 8$ which indicates that the quenching is due to dipole-quadrupole interaction for both the NPs.

Selection rules permit magnetic dipole (MD) transition while dipole transition (ED) is forbidden. However, J-mixing due to the crystal field perturbation by the host matrix enables such forbidden This happens in the cases .transitions in which local symmetry of the activators does not include an inversion centre. Hence such transitions ($^5D_0 \rightarrow {}^7F_2$) are termed as induced electric dipole transitions. For this reason, the emission intensity ratio between ED and MD transitions called asymmetry ratio is used as a measure of degree of distortion from inversion symmetry of the local environment surrounding the Eu^{3+} ions in the host matrix.

The ratios of integrated intensities of ED ($^5D_0 \rightarrow {}^7F_2$) to MD ($^5D_0 \rightarrow {}^7F_1$) transitions can be used to determine the symmetry of Eu^{3+} ions in the matrix and is called asymmetric ratios.

$$\text{Asymmetric ratio} = \frac{\int I_{ED} d\lambda}{\int I_{MD} d\lambda} \qquad (6)$$

.The ratio of intensity of I_{ED}/I_{MD} remains almost constant, which indicates that the introduction of Eu^{3+} ions into Y_2SiO_5 mainly located in sites with inversion symmetry in nanophosphor calcined at 1100 ^{0}C as well as at 1300 ^{0}C.

CIE coordinates are estimated from 1931 CIE (International Commission on Illumination) system for $Y_2SiO_5:Eu^{3+}$) $^+$1-9 mol (%NPs. Fig. 4a) and Fig. 4b) show CIE plots of $Y_2SiO_5:Eu^{3+}$(1-9 mol %) calcined at 1100 ^{0}C and at 1300 ^{0}C respectively. The colour matching functions used in the calculation of tristimulus values X, Y and Z, were taken from [21]. It was observed that the CIE colour co-ordinates lie in strong red region for both the NPs .To identify technical applicability of this red emission, CCT is determined from the CIE co-ordinates. CCT specify colour appearance of the light emitted by a light source, relating its colour to the colour of light from a reference source, when heated to a particular temperature. For the NPs calcined at 1100 ^{0}C (Fig. 4(c)) the correlated colour temperature is found to be 1806 K and for the one calcined at 1300 ^{0}C it is found to be 1776 K (Fig. 4(d)). The color purity was calculated using the relation;

$$\text{color purity} = \frac{\sqrt{(x_s - x_i)^2 + (y_s - y_i)^2}}{\sqrt{(x_d - x_i)^2 + (y_d - y_i)^2}} \qquad (7)$$

where (x, y) are the coordinates of the sample point, (x_i, y_i) are the coordinates of illumination points and (x_d, y_d) are the coordinates of the dominant wavelength. The CIE co-ordinates and color purity of the samples at various dopant concentration are tabulated in Table 2 and 3. Calculated CCT co-ordinates are tabulated in Table 4.

Table 2: CIE coordinates of $Y_2SiO_5:Eu^{3+}$ Calcined at 1100 ^{0}C (1-9 mol %)

Concentration (Mole fraction)	x	y	Colour purity (%)
0.01	0.586	0.405	97.99
0.03	0.607	0.388	98.74
0.05	0.614	0.383	99.40
0.07	0.611	0.384	98.88
0.09	0.614	0.383	99.31

Table 3: CIE coordinates of $Y_2SiO_5:Eu^{3+}$ Calcined at 1300^{0}C (1-9 mol %)

Concentration (Mole fraction)	x	y	Colour purity (%)
0.01	0.586	0.407	98.49
0.03	0.594	0.395	97.36
0.05	0.594	0.395	97.43
0.07	0.609	0.385	98.72
0.09	0.611	0.386	99.35

Table 4: CCT coordinates of $Y_2SiO_5:Eu^{3+}$ (1-9 mol %)

	$Y_2SiO_5:Eu^{3+}$ (1-9 mol %) calcined at 1100 ^{0}C			$Y_2SiO_5:Eu^{3+}$ (1-9 mol %) calcined at 1300 ^{0}C		
Mol %	u'	v'	CCT (k)	u'	v'	CCT (K)
1	0.350	0.545	1757	0.349	0.545	1760
3	0.376	0.542	1788	0.362	0.542	1752
5	0.385	0.541	1834	0.362	0.542	1752
7	0.382	0.541	1818	0.380	0.541	1806
9	0.385	0.541	1834	0.381	0.542	1808

3.3.Judd Ofelt Analysis

Judd Ofelt theory is generally used to analyse the spectral intensities quantitatively. The local environment of Eu^{3+} ion affects the JO parameter Ω_2. It is also enhanced by covalence of Eu – O bonds. The electron density around the lanthanide ion influences the JO parameter Ω_4 and Ω_6 determines the rigidity of the host material. The analysis was

carried out following the reference [22]. The reduced matrix elements are also taken from the reference [22]. Using the measured values and predicted values of line strength, we employed least square fit method to calculate the Judd Ofelt intensity parameters. The calculated JO intensity parameters for the entire sample are tabulated in Table. 5 and 6.

Table 5: JO intensity parameters (in 10^{-20}cm^2 units) of $Y_2SiO_5:Eu^{3+}$ (1-9 mol %) calcined at 1100 ^{0}C

Concentration (Mol %)	Ω_2	Ω_4	Ω_6	Asymmetric ratio
1	1.90	1.30	0.04	2.160
3	0.22	0.63	0.04	0.718
5	2.86	4.20	0.13	1.602
7	0.20	0.32	0.02	2.067
9	0.32	0.17	0.03	0.794

Table 6: JO intensity parameters (in 10^{-20}cm^2 units) of $Y_2SiO_5:Eu^{3+}$ (1-9 mol %) calcined at 1300 ^{0}C

Concentration (Mol %)	Ω_2	Ω_4	Ω_6	Asymmetric ratio
1	3.31	2.55	0.12	3.414
3	1.50	1.96	0.04	2.219
5	1.15	0.65	0.03	2.049
7	5.43	2.29	0.07	3.234
9	1.33	1.16	0.04	0.528

The values of the line strength S_{ED}, transitions probabilities A_{ED} A_{MD} and branching ratio β_{cal}, for the nanophosphor in both the phases (1 mol% of Eu^{3+} in X1 phase and 3 mol% of Eu^{3+} in X2 phase) are tabulated in Table 7 and 8.

Table 7: Calculated line strength$\times 10^{-22}$ cm^2, transition probabilities (s^{-1}), branching ratios in $Y_2SiO_5:Eu^{3+}$ (5 mol %) calcined at 1100 ^{0}C

Transition	λ(nm)	S_{ED}	A_{ED}	A_{MD}	β
$^5L_9$ - $^7F_0$	354	0.0012	5.61	2.430	0.4582
$^5D_4$ - $^7F_0$	361	0.0782	706.	0.000	0.7045
$^5G_6$ - $^7F_0$	369	0.0065	37.7	0.000	0.9289
$^5G_4$ - $^7F_0$	376	0.0076	60.7	0.000	0.9583
$^5G_2$ - $^7F_0$	383	0.0000	0.00	3034.	0.9996
$^5L_6$ - $^7F_0$	392	0.0191	93.2	0.000	0.9796
$^5D_3$ - $^7F_0$	407	0.0000	0.00	6.849	0.8040
$^5D_0$ - $^7F_0$	576	0.0099	198.	0.000	1.0000

It is evident from the obtained values that the asymmetric ratio for 5 mol % is close to 1 for the sample calcined at 1100 ^{0}C suggesting that both MD and ED transitions are equally probable. For the sample calcined at 1300 ^{0}C asymmetric ratio decreased with the dopant concentration, indicating that ED dominated over MD. The decrease in asymmetric ratio with the dopant concentration indicates that ED dominated over MD transitions [23].

Table 8: Calculated line strength $\times 10^{-20}$ cm^2, transition probabilities (s^{-1}), branching ratios in $Y_2SiO_5:Eu^{3+}$ (7 mol %) calcined at 1300 ^{0}C

Transition	λ(nm)	S_{ED}	A_{ED}	A_{MD}	β
$^5L_9$ - $^7F_0$	352	0.0012	5.52	0.000	0.8565
$^5D_4$ - $^7F_0$	360	0.0006	5.60	0.000	0.9923
$^5L_8$ - $^7F_0$	364	0.0072	33.8	0.028	0.8120
$^5G_6$ - $^7F_0$	370	0.0037	21.4	0.000	0.7763
$^5G_4$ - $^7F_0$	374.	0.0000	0.00	1809.4	0.9990
$^5G_2$ - $^7F_0$	383	0.0042	57.2	125.61	0.9287
$^5D_3$ - $^7F_0$	407	0.0176	142.	0.000	0.9993
$^5D_0$ - $^7F_0$	580	4.4276	867	15067.	1.0000

From the values of asymmetric ratio, one can infer that Ω_2 values shows non-symmetrical nature and hence lacks inversion symmetry. The JO parameters are higher at 1 mol % of Eu^{3+} in host lattice when calcined at 1100 ^{0}C and at 3 mol % of Eu^{3+} in host lattice when calcined at 1300 ^{0}C, indicating the dominance of the crystal field on the ions that results in intense ED transition. Furthermore, it is practically evident that in order to treat Eu^{3+} phosphors as potential candidates for red emission, the intensity corresponding to $^5D_0 \rightarrow {}^7F_2$ should be dominant over $^5D_0 \rightarrow {}^7F_1$ for better colour emission and colour purity. This is evident from the values of JO parameters obtained for nanoparticles calcined at both the temperatures and for all dopant concentrations.

It can be seen that the Ω_2 parameter of the synthesized nanophosphor in X1 phase is smaller than that in X2 phase. The smaller value of Ω_2 in X1 phase may indicate that the Eu─YNO_3 bonds have a smaller covalence bond than other RE─anion bonds in that phase. It is found that the spectroscopic quality factor, χ values for all the samples is very much greater than one. We observed that the trend for JO parameters for our samples are $\Omega_2 > \Omega_4 > \Omega_6$ for sample in X2 phase. The value of Ω_2 is small in magnitude which implies that the strength of asymmetry is lower in the vicinity of the rare-earth ions. The value of Ω_6, which is very much smaller in our case, is related to the density of 6s electrons that shield the 4f electrons responsible for the optical transition of Ln^{3+} [24]. Due to effective shielding of 4f

shell by fully filled 5s and 5p orbitals, the electronic cloud experiences very weak ligand field influences. Although weak, this perturbation is responsible for the 4f intra-configurational electric dipole transitions.

3.4.PL Excitation Spectra

Fig. 5 (a) and 5 (b) show PL excitation spectra of $Y_2SiO_5:Eu^{3+}$ nanophosphor calcined at 1100 ^{0}C and 1300 ^{0}C respectively, with emission wavelength maintained at 612 nm. The excitation spectra of Europium (III) compounds allow the determination of the higher energy levels of the $4f^6$ electronic configuration of the Eu^{3+} ion. The absorption peaks were observed at wavelengths 357 nm, 368 nm, 387 nm, 408 nm, 417 nm, 449 nm, 460 nm, 468 nm, and 485 nm. The corresponding transitions are identified as $^5D_4 \leftarrow {}^7F_0$, $^5D_4 \leftarrow {}^7F_1$, $^5L_7 \leftarrow {}^7F_1$ / $^5L_6 \leftarrow {}^7F_0$, $^5L_6 \leftarrow {}^7F_1$, $^5D_3 \leftarrow {}^7F_1$, $^5D_3 \leftarrow {}^7F_3$, $^5D_2 \leftarrow {}^7F_0$, $^5D_2 \leftarrow {}^7F_0$, and $^5D_2 \leftarrow {}^7F_1$ / $^5D_2 \leftarrow {}^7F_2$.

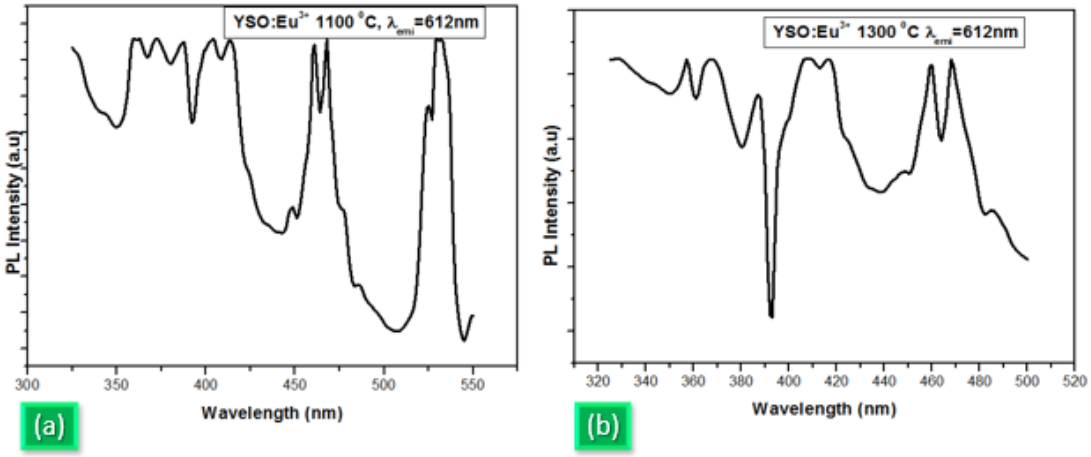

Fig. 5 PL excitation spectrum of $Y_2SiO_5:Eu^{3+}$ (7 mol %) a) calcined at 1100 ^{0}C b) calcined at 1300 ^{0}C

The transition $^5D_3 \leftarrow {}^7F_1$ is a magnetic dipole transition and $^5D_3 \leftarrow {}^7F_3$ is a very strong electric dipole transition. Spectra measured at room temperature allow observing transitions starting from the $^7F_1$ and even from the $^7F_2$ excited state. Some of these transitions are to energy levels that cannot be reached from the ground state $^7F_0$, since they are forbidden by the selection rules for the point symmetry group of the Eu^{3+} site. The transitions from the $^7F_1$ level are weaker than those of the $^7F_0$ level.

3.5.Diffuse Reflectance Spectra

The diffuse reflectance spectra of $Y_2SiO_5:Eu^{3+}$ (1-9 mol %) NPs were shown in the Fig. 6(a) and 6(b) respectively. A strong absorption spectrum was observed with peaks at 210, 257 and 384 nm. The sharp absorption peaks observed at 210 nm arise due to charge transfer state transition between valence band to conduction band, i.e., between O^{2-} to Eu^{3+}. The weak absorption band at ~ 257 nm region was expected to arise from transitions involving extrinsic states such as surface traps / defect states / impurities [25]. Another absorption peak observed at 384 nm was due to intra-configurational transitions in Eu^{3+}.

The band gap in the nanomaterials can be found using DRS according to the Kubelka-Munk relation

$$\frac{K}{S} = \frac{(1-R_\infty)^2}{2R_\infty} \equiv F(R_\infty) \qquad (8)$$

R_∞ is the Kubelka-Munk function, and $R_\infty = \frac{R_{sample}}{R_{standard}}$. In the parabolic band structure, the band gap Eg, and absorption coefficient α of a direct band gap semiconductor are related through the well-known equation [26].:

$$\alpha h\nu = C_1(h\nu - E_g)^{1/2} \qquad (9)$$

where α is the linear absorption coefficient of the material, $h\nu$ is the photon energy and C_1 is a proportionality constant. When the material scatters in perfectly diffused manner (or when it is illuminated at 60^0 incidence), the K-M absorption coefficient K becomes equal to 2α. In this case, considering the K-M scattering coefficient S as constant with respect to wavelength, and using the remission function we obtain the expression:

$$[F(R_\infty)h\nu]^2 = C_2(h\nu - E_g) \qquad (10)$$

Therefore, obtaining $F(R_\infty)$ from Eq. (2) and plotting $[F(R_\infty)h\nu]^2$ against $h\nu$, the band gap E_g of a powder sample can be extracted easily. The direct band gap was calculated for the nanophosphor synthesized sonochemically and calcined at 1100 ^{0}C was found to be in the range of 5.43 – 5.56 eV. For the nanophosphor calcined at 1300 ^{0}C the bandgap was estimated to be in the range of 5.27eV-5.57eV. With

the increase in Eu^{3+} concentration from 1 – 9 mol %, the band gap was found to increase a little. A plausible explanation for the variations observed in the Eg values can be related to the degree of structural order–disorder into the lattice, which is able to change the intermediary energy-level distribution within the band gap. The Eg values mainly depend on the preparation methods and experimental conditions. In particular, these key factors can favour on inhibit the formation of structural defects which are able to control the degree of structural order–disorder of the material and, consequently, the number of intermediary energy levels within the band gap. It was observed that the absorption measurements were extremely sensitive to the changes in the lattice or variations on the structural order–disorder degree [27].

of X1 phase. Thus, for luminescence properties of YSO: Eu^{3+} is better in X2 phase than in X1 phase.

From the results, it is observed that the maximum intensity of red emission was found to be for the dopant concentration of 5mol % when calcined at 1100 ^{0}C and 7 mol % when calcined at 1300 ^{0}C. Concentration quenching is due to multipolar dipole-quadrupole interaction. Asymmetric ratio is more than 1, the high value infers that radiative transition dominates over non-radiative ones. For the nanophosphor in X1 phase asymmetric ratio is small for 3 mol % of the dopant concentration. For the nanophosphor in X2 phase the asymmetric ratio decreases with the increase in the dopant concentration. Higher the value of asymmetric ratio higher the asymmetry in the environment of Eu^{3+} [28]. The

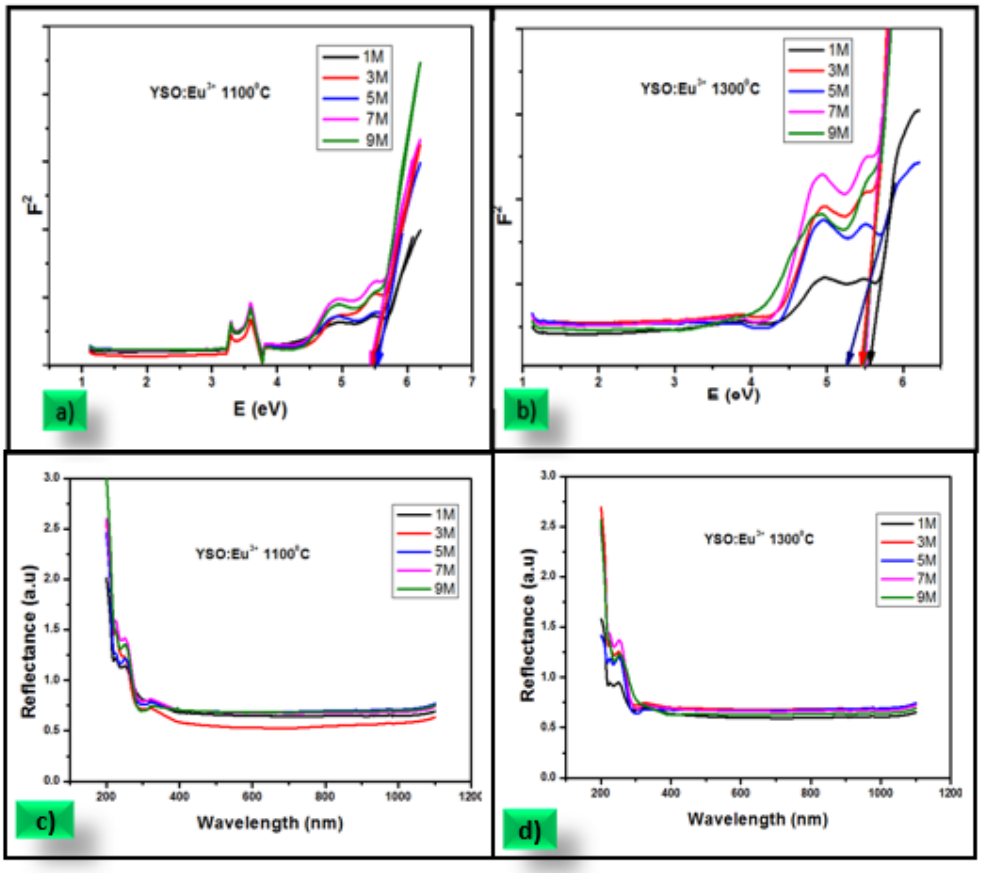

Fig. 6a) Plot of F^2 Vs E for $Y_2SiO_5:Eu^{3+}$ (1-9 mol %) calcined at 1100^{0}C b) Plot of F^2 Vs E for $Y_2SiO_5:Eu^{3+}$ (1-9 mol %) calcined at 1300^{0}C c) Reflectance spectra of $Y_2SiO_5:Eu^{3+}$ (1-9 mol %) calcined at 1100^{0}C d) Reflectance spectra of $Y_2SiO_5:Eu^{3+}$ (1-9 mol %) calcined at 1300^{0}C

4 Conclusions

It is evident from the table that the Ω_2 parameter is large at 5 mol % of dopant concentration in phase X1 and at 7 mol % of dopant concentration in phase X2. We also found that JO intensity parameters for the nanophosphor at X2 phase are more than that

CIE colour coordinates lie in strong red region for both the compounds. The correlated colour temperature of the nanophosphor is found to be 1806 K for X1 phase and it is 1776 K for X2 phase. The Ω_2 parameters and other parameters like bandwidth, optical gain, line strength for the compound we prepared via sonochemical method are many orders

more than the compound prepared by other conventional methods. Thus, the synthesised nanophosphor is an efficient candidate for luminescent applications.

5 Reference

1. E. Coetsee, J.J. Terblans, O.M. Ntwaeaborwa, H.C. Swart, Physica B 404 (2009) 4426–4430, doi: 10.1016/j.physb.2009.09.015.
2. Ramachandra Naik, S.C. Prashantha, H. Nagabhushana, S.C. Sharma, B.M. Nagabhushana, H.P. Nagaswarupa, H.B. Premkumar, Sens. Actuat. B 195 (2014) 140–149.
3. P.J. Marsh, J. Silver, A. Vecht, A. Newport, J. Lumin. 97 (2002) 229–236. doi:10.1016/S0022-2313(02)00229-6.
4. Parganiha, Y., Kaur, J., Dubey, V., & Chandrakar, D. (2015). 77, 152–161. doi:10.1016/j.spmi.2014.11.010.
5. Petoud, S., Cohen, S. M., Bünzli, J.-C. G., & Raymond, K. N. (2003), Journal of the American Chemical Society, 125(44), 13324–13325. doi:10.1021/ja0379363.
6. Lenaerts, P., Driesen, K., Van Deun, R., & Binnemans, K. (2005). Chemistry of Materials, 17(8), 2148–2154. doi:10.1021/cm0486868.
7. Li, H. R., Lin, J., Zhang, H. J., Fu, L. S., Meng, Q. G., & Wang, S. B. (2002). Chemistry of Materials, 14(9), 3651–3655. doi:10.1021/cm0116830.
8. Binnemans, K., & Görller-Walrand, C. (2002). Lanthanide-Containing Liquid Crystals and Surfactants. Chemical Reviews, 102(6), 2303–2346. doi:10.1021/cr010287y.
9. Sahu, I. P., Chandrakar, P., Baghel, R. N., Bisen, D. P., Brahme, N., & Tamrakar, R. K. (2015). Journal of Alloys and Compounds, 649, 1329–1338. doi:10.1016/j.jallcom.2015.06.011
10. Wu, Q., Jing, X., & Jiao, H. (2009). Optical Materials, 31(8), 1123–1127. doi:10.1016/j.optmat.2008.12.004.
11. Santosh K. Gupta, M. Kumar, V. Natarajan, S.V. Godbole, Opt. Mater. 35 (2013) 2320–2328.
12. Rambabu, U., & Han, S.-D. (2013). Materials Research Bulletin, 48(2), 512–520. doi:10.1016/j.materresbull.2012.11.004.
13. Z.H. Zhang, Y.H. Wang, Y. Hao, W.J. Liu, J. Alloys Compd. 433 (2007) L12–L14.
14. K. S. Suslick, Ultrasound: Its Chemical, Physical, and Biological Effects, Wiley-VCH, New York 1988.
15. B. S. Ravikumar, H. Nagabhushana, S. C. Sharma, Y. S. Vidya, K. S. Ananatharaju, Spect.chem Acta A, 136 (2015) 1027-1037
16. Gurushantha, K., L. Renuka, Anantharaju, K. S., Vidya, Y. S., Nagaswarupa, H. P., Prashantha, S. C., & Nagabhushana, H. (2017). Materials Today: Proceedings, 4(11), 11747–11755. doi:10.1016/j.matpr.2017.09.091
17. Hölsä, J., Jyrkäs, K., & Leskelä, M. (1986). Journal of the Less Common Metals, 126, 215–220. doi:10.1016/0022-5088(86)90283-3.
18. Y. S. Vidya, K. Gurushantha, H. Nagabhushana, S. C. Sharma, K. S. Anantharaju, C. Shivakumara, D. Suresh, H. P. Nagaswarupa, S. C. Prashantha, M. R. Anilkumar, J. Alloys Compds. 622 (2015) 86.
19. Kirby, A. F., & Richardson, F. S. (1983). The Journal of Physical Chemistry, 87(14), 2544–2556. doi:10.1021/j100237a018.
20. P.B. Devaraja, D.N. Avadhani, S.C. Prashantha, H. Nagabhushana, S.C. Sharma, B.M. Nagabhushana, H.P. Nagaswarupa, Spectr. Acta Part A: Mol. Bio. Spectr. 121 (2014) 46-52.
21. Claudio Oleari, Standard Colorimetry Definitions, Algorithms and Software, John Wiley & Sons, Ltd, 2016, ISBN: 9781118894446.
22. B.M. Walsh, "Judd-Ofelt Theory: Principles and Practices" in Advances in Spectroscopy for Lasers and Sensing, ed. B. Di Bartolo and O. Forte (Springer, Netherlands, 2006) 403-433.
23. C. Manjunath∗, M.S. Rudresha, R. Hari Krishna, B.M. Nagabhushana, B.M. Walsh, K.R. Nagabhushana, B.S. Panigrahi, Optical Materials 85 (2018) 363–372
24. Hölsä, J., & Porcher, P. (1982). The Journal of Chemical Physics, 76(6), 2790–2797. doi:10.1063/1.443381
25. Y. S. Vidya, K. S. Anantharaju, H. Nagabhushana, S. C. Sharma, J. Alloys Compd. 619 (2015) 760-770
26. Y. S. Vidya, B. N. Lakshminarasappa, Synthesis, J. Lumin. Apps, 1 (2014) 40
27. Vidya, Y. S., & Lakshminarasappa, B. N. (2014). Applied Physics A, 118(1), 249–260. doi:10.1007/s00339-014-8669-8.
28. M. Shivram, S.C. Prashantha, H. Nagabhushana, S.C. Sharma, K. Thyagarajan, R. Harikrishna, B.M. Nagabhushana, Spectr. Acta Part A: Molec. Biom. Spectr. 120 (2014) 395–400.